

Hinode/Extreme-Ultraviolet Imaging Spectrometer Observations of the Temperature Structure of the Quiet Corona

David H. Brooks^{1,2,3}, Harry P. Warren¹, David R. Williams^{3,4}, Tetsuya Watanabe⁵

dhbrooks@ssd5.nrl.navy.mil

ABSTRACT

We present a Differential Emission Measure (DEM) analysis of the quiet solar corona on disk using data obtained by the Extreme-ultraviolet Imaging Spectrometer (EIS) on *Hinode*. We show that the expected quiet Sun DEM distribution can be recovered from judiciously selected lines, and that their average intensities can be reproduced to within 30%. We present a subset of these selected lines spanning the temperature range $\log T = 5.6$ to 6.4 K that can be used to derive the DEM distribution reliably, including a subset of Iron lines that can be used to derive the DEM distribution free of the possibility of uncertainties in the elemental abundances. The subset can be used without the need for extensive measurements and the observed intensities can be reproduced to within the estimated uncertainty in the pre-launch calibration of EIS. Furthermore, using this subset, we also demonstrate that the quiet coronal DEM distribution can be recovered on size scales down to the spatial resolution of the instrument ($1''$ pixels). The subset will therefore be useful for studies of small-scale spatial inhomogeneities in the coronal temperature structure, for example, in addition to studies requiring multiple DEM derivations in space or time. We apply the subset to 45 quiet Sun datasets taken in the period 2007 January to April, and show that although the absolute magnitude of the coronal DEM may scale with the amount of released energy, the shape of the distribution is very similar up to at least $\log T \sim 6.2$ K in all cases. This result is consistent with the view that the *shape* of the quiet Sun DEM is mainly a function of the radiating and

¹Space Science Division, Code 7673, Naval Research Laboratory, Washington, DC 20375

²George Mason University, 4400 University Drive, Fairfax, VA 22020

³Present address: Hinode Team, ISAS/JAXA, 3-1-1 Yoshinodai, Sagamihara, Kanagawa 229-8510, Japan

⁴Mullard Space Science Laboratory, University College London, Holmbury St Mary, Dorking, Surrey, RH5 6NT, UK

⁵National Astronomical Observatory of Japan, Osawa, Mitaka, Tokyo 181-8588, JAPAN

conducting properties of the plasma and is fairly insensitive to the location and rate of energy deposition. This *universal* DEM may be sensitive to other factors such as loop geometry, flows, and the heating mechanism, but if so they cannot vary significantly from quiet Sun region to region.

Subject headings: Sun: UV radiation—Sun: corona—Techniques: spectroscopic

1. Introduction

Since the advent of space based solar EUV and X-ray observations, spectroscopic diagnostic techniques have been used to measure solar plasma properties such as the electron density, velocity, chemical composition, or coronal temperature structure. These quantities are useful inputs to physical models and provide confirmation of theoretical predictions.

The differential emission measure (DEM) technique is widely employed for studying the distribution of material as a function of temperature. It is also used for validation of atomic data, spectral line identification, measurements of elemental abundances, instrument radiometric calibration, or to compare with theoretical models. All these methods, however, rely on a number of physical assumptions that may not be realistic for the target under investigation. It is important, therefore, to understand the limitations of the diagnostic capabilities of the techniques so that the measurements can be interpreted correctly.

In recent years, orbiting instrument capabilities have reached the point where spatially resolved structures in the solar atmosphere can be examined spectroscopically. Variations of the DEM and emission measure techniques have been used to try to shed light on the coronal loop controversy: are loops isothermal? (Lenz et al. 1999; Aschwanden et al. 1999, 2000) or multi-thermal? (Schmelz et al. 2001; Warren et al. 2008), to study the validity of complex multiple peaked DEM distributions in active regions (Brosius et al. 1996; Lanzafame et al. 2002), and to study spatial inhomogeneities in the quiet coronal DEM distribution (Lanzafame et al. 2005). Most recently, DEM analysis has been applied to observations from the Extreme ultraviolet Imaging Spectrometer (EIS, Culhane et al. 2007) on *Hinode* (Kosugi et al. 2007).

Previous studies of small-scale spatial inhomogeneities in the quiet coronal DEM distribution have suggested that the shape of the DEM is very similar up to $\log T_e = 6.1$ K when it is derived from intensities averaged over large enough areas (Lanzafame et al. 2005). If confirmed, this is potentially an important result because it provides a further constraint on the heating. Our interest here is to extend this analysis of small-scale spatial variations in the quiet coronal DEM to multiple regions observed at different locations and different

times and therefore examine in detail whether this result is true in general.

For ambitious studies that require derivation of the DEM distribution multiple times, this can be time consuming when many lines are included in the analysis. For the EIS data, 276 spectral lines were identified in the 171–212 Å and 245–291 Å wavelength ranges by Brown et al. (2008) and each line would need careful fitting prior to a DEM study. It is of interest therefore to produce a subset of spectral lines that can be used to reliably derive the DEM in multiple locations or at many different times.

EIS also has the capability to derive the DEM distribution using spectral lines of Fe ions only, thus allowing an abundance uncertainty free analysis (Watanabe et al. 2007). In addition, Fe ions have the advantage that they relax into ionization equilibrium faster than ions of other species (Lanzafame et al. 2002) which could be helpful for probing the assumptions underlying the technique. It is also of interest, therefore, to emphasize Fe when selecting reduced subsets of reliable spectral lines.

It is well known, however, that current atomic modeling of this complex atom is insufficiently advanced compared to that of lighter species (Summers et al. 2006), and recent analysis of EIS data has indicated significant uncertainty in the ionization equilibrium calculations for Fe (Young et al. 2007a) and modeling of the weaker emission lines. In order to achieve our aims, we need to have confidence in the atomic data used for the analysis, and to examine the spectra in detail to understand which lines are the best candidates for detailed analysis. In addition, one needs to have confidence that the photometric calibration performed in the laboratory can be used reliably on orbit.

In this paper, we first examine a spectral atlas prepared from EIS observations of a very quiet region observed on 2007 January 30. A quiet coronal region was chosen so that comparison could be made to previous coronal DEM distributions derived from quiet Sun data. Here we compare with the DEM distribution obtained by Brooks & Warren (2006) using Solar and Heliospheric Observatory (SOHO, Domingo et al. 1995) Coronal Diagnostic Spectrometer (CDS, Harrison et al. 1995) observations. We derive the DEM distribution using the most reliable lines and apply that solution to a larger linelist to identify problematic issues with line fitting, atomic data etc. We then produce a subset of lines, with one recommended line at each temperature, that can be used to recover the same DEM solution. This subset can be used without the need for extensive measurements and contains a series of lines from Fe ions that can be used to derive the DEM removing the possibility of uncertainties due to elemental abundances. We also demonstrate here that EIS is an ideal instrument for studying inhomogeneities in the DEM distribution because its sensitivity allows us to derive the same coronal DEM on very small spatial scales (down to a single EIS 1" pixel).

We then apply our best-case EIS DEM solution to 45 full-CCD quiet Sun datasets and explore the possibility that it can reproduce the observed intensities of the subset of lines in each observation. We find that in the vast majority of the cases the DEM is very similar up to at least $\log T_e = 6.15$ K with only minor adjustments to the shape and some re-scaling of the magnitude.

In §2 we describe the observations studied and data reduction techniques used. In §3 we reference the atomic data adopted. In §4 we describe the DEM method and specifics of our analysis. In §4.3 we discuss our analysis strategy. In §5 we present our results and in §7 we summarize the paper and discuss the implications of our findings.

2. Observations and Data Reduction

Hinode made observations of a quiet region close to disk center on 2007 January 30. Figure 1 shows an EIT 195 Å full-disk image taken at 13:13:40UT with the EIS study field-of-view overlaid. The FOV is $128'' \times 128''$ and was built up by stepping the $1''$ slit from solar West to East over a 3 1/2 hour period from 14:34:40 to 18:00:00UT. The study takes full spectra on both the EIS detectors from 171-212 Å and 245-291 Å. The exposure time was 90s and the study acronym is HPW001_FULLCCD_RAST. The data were taken during the daily long SAA (South Atlantic Anomaly) free period around the *Hinode* orbit.

Figure 2 shows example images formed from Gaussian line fits to the EIS data. Examples using Si VII 275.352 Å, Fe X 185.213 Å, Fe XII 195.119 Å, and Fe XV 284.160 Å are shown. These lines are formed in the temperature range $\log T_e = 5.7$ to 6.35 K. Both Figures 1 and 2 indicate that the region of quiet corona selected is indeed free of any significant activity.

The EIS data require removal of the CCD dark current, cleaning for cosmic-ray strikes on the CCD, and processing of the data to take account of hot, warm, and dusty pixels. In addition, the radiometric calibration needs to be applied to convert the data from photon events to physical units. In this work we have applied these corrections and calibrations using the EIS software routine *EIS_PREP* that is available in SolarSoft. Average line profiles over the full $128''$ in the X- and Y- directions were constructed to improve the signal-to-noise and provide a spectral atlas for analysis.

The EIS CCDs were slightly offset from each other by 1–2 pixels in -X prior to an adjustment to the slit assembly position on 2008, August 24. In addition, there is an offset between the CCDs of ~ 18 pixels in -Y (wavelength dependent). No major difference is expected to be introduced, however, by ignoring these offsets for the spectral atlas: on disk quiet Sun intensities typically do not vary significantly when averaged over large spatial areas.

Using the Fe lines from the final subset (see §5.3), we verified that in these observations the detector offsets typically introduce a variation of less than 15% to the averaged line intensities. The offsets are clearly important for velocity analysis and accurate measurements in small areas, so we have taken the appropriate values into account for the DEM analysis of the single pixel measurements (see §5.4).

3. Atomic Data

In this work, we use the CHIANTI database version 5.2 (Dere et al. 1997; Landi et al. 2006). Details of the sources of the electron collisional excitation, deexcitation, and spontaneous radiative decay rates, are given in the database and accompanying papers. The zero density ion fractional abundances of Mazzotta et al. (1998) are used throughout the paper, together with the coronal elemental abundances of Feldman et al. (1992).

4. Differential Emission Measure

Assuming a constant electron pressure as the basis of a relationship between electron temperature and density, an optically thin emission line intensity arising from a transition between two atomic levels can be written as

$$I_{nl} = A(Z) \int_{T_e} G_{nl}(T_e, N_e) \phi(T_e) dT_e \quad (1)$$

where n and l denote the levels, $A(Z)$ is the elemental abundance of the atomic species, N_e and T_e are the electron density and temperature, $\phi(T_e)$ is the emission measure differential in temperature, and $G(T_e, N_e)$ is the contribution function. The latter is a function of temperature and density but is calculated in this work at a specific electron pressure estimated from a density sensitive line ratio in §4.2. The results of that measurement justify the neglect of density effects for the very quiet region studied in this work.

4.1. Method

We represent the emission measure curve with a series of spline knots as in Warren (2005) and Brooks & Warren (2006). These knots can be interactively moved to control the smoothness of the emission measure distribution and this has been found to be helpful in the past for representing the rapid fall-off of emission measure at high temperatures in the quiet

corona. The values of the knots are determined from a χ^2 minimization of the differences between the measured intensities and those calculated from the DEM distribution.

4.2. Coronal Electron Pressure

As discussed above, we need to make an electron density measurement using line ratios in order to calculate the contribution functions that are needed for the DEM analysis. The EIS wavelength range contains a number of excellent density sensitive line ratios and some of these have been assessed in detail by Young et al. (2009). Here we use the Fe XII 186.8 Å to Fe XII 195.119 Å ratio that is sensitive in the density range $\log N_e = 8\text{--}12 \text{ cm}^{-3}$.

Young et al. (2007a) note that the Fe XII 186.8 Å line is a self-blend of lines at 186.88 Å and 186.856 Å and is also blended with S XI 186.839 Å. They also note that the contribution from the S XI 186.839 Å line can be estimated by taking the ratio of that line to the S XI 191.264 Å line. This ratio has a fixed value of 0.2. Furthermore, the Fe XII 195.119 Å line has been found to be broader in EIS spectra than the Fe XII 193.515 Å line (Young et al. 2007a), indicating a possible Fe XII blend at 195.18 Å as suggested by Del Zanna & Mason (2005). If present, this blend should only be significant at high densities (Del Zanna & Mason 2005) and should only contribute $\sim 10\%$ to the main feature at densities of $\log N_e = 10 \text{ cm}^{-3}$ (Young et al. 2007a).

We measured the intensity of the S XI 191.264 Å line in order to estimate the contribution of the S XI 186.839 Å line to the component identified as Fe XII 186.8 Å. We then calculated the spread in the diagnostic line ratio values that would be obtained if we included or excluded this blend and also included or excluded a 10% modification to the Fe XII 195.119 Å line intensity arising from the possible blend at 195.18 Å. The measured ratios spread from 0.12–0.15 and these values translate to a spread in electron density of $\log N_e = 8.4\text{--}8.5 \text{ cm}^{-3}$ or electron pressure of $\log P_e = 14.5\text{--}14.65 \text{ cm}^{-3} \text{ K}$. These values are in good agreement with the quiet coronal electron pressure calculated from Si X and Si XI line ratios by Brooks & Warren (2006) and also with previous measurements by Young (2005) and Warren (2005). Thus the blends do not appear to significantly affect our measurements with this ratio and we therefore adopt a value of $\log P_e = 14.5 \text{ cm}^{-3} \text{ K}$ for calculating the contribution functions.

4.3. Line Selection Strategy

We used the comprehensive spectral line identification study of Brown et al. (2008) to identify 276 lines in our quiet Sun dataset. Brown et al. (2008) state that those lines with greater than 20DN per 60s exposure have good precision in their Gaussian fitting. Therefore, we excluded lines with lower count rates from our analysis with the exception of the following four: Ne V 184.73 Å, O IV 279.631 Å, O IV 279.933 Å, and O VI 183.937 Å. These lines were included in the hope of stabilizing the DEM distribution at lower temperatures: the vast majority of the spectral lines in the EIS wavelength range are formed at upper transition region and coronal temperatures. In addition, referring to the first results analysis of the EIS spectra of Young et al. (2007a) and again to Brown et al. (2008) we excluded lines that had been identified as blended in either study. Thus the following 19 lines were excluded: Ar XI 184.501 Å, Fe XII 186.880 Å, Ar XIV 187.954 Å, Fe XI 189.125 Å, Fe XI 189.940 Å, Fe XI 190.886 Å, S XI 191.260 Å, Fe XIV 192.629 Å, Fe XI 192.811 Å, Fe XI 192.913 Å, Fe XIV 193.270 Å, Fe XII 196.645 Å, Fe XI 198.550 Å, Fe XIII 201.122 Å, Fe X 256.434 Å, Fe XII 259.491 Å, Si VII 276.863 Å, Mg VII 277.021 Å, and Mg VII 278.410 Å. Finally, the following three Fe IX lines, recently proposed as identifications by Young (2009), were added to our line list in the hope of filling in the temperature range at the base of the corona: Fe IX 188.485 Å, Fe IX 189.940 Å, and Fe IX 197.858 Å. The 188.485 Å and 189.940 Å features were identified with lines of Fe XII and Fe XI, respectively, by Brown et al. (2008). Each of the remaining 77 lines were fitted using the Brown et al. (2008) analysis as a reference guide for the positions of spectral features in the spectrum.

The spectral ranges selected were fitted with multiple Gaussians plus a polynomial background using a line fitting software package developed by the authors that utilizes the IDL routine *MPFIT* (Markwardt 2009).

After completing this process we further inspected the reliability of the line fits that were made. Our intention was to try to derive a DEM distribution that could reproduce the observed intensities to an accuracy level that was comparable to that obtained for previous spectrometers. Therefore, we decided to initially select only those lines, the intensities of which were measured to extremely high precision. After deriving the DEM distribution for these lines we would then apply the solution to the complete set of spectral lines. In addition, the following lines were excluded because no suitable atomic data were available: Ni XI 186.978 Å, Fe XI 192.014 Å, Fe VII 196.054 Å, Ni XIV 196.226 Å, Ni XIV 200.692 Å, Fe XIII 202.424 Å, the following two lines were excluded because the lines were too weak to fit reliably in our spectrum: S XIII 256.684 Å, Fe XVI 262.983 Å, and the He II 256.332 Å line was excluded because it is unlikely to be optically thin.

The final set of 29 lines for our first DEM attempt is given in Table 1 and the DEM

results are discussed in §5.

5. Results

Here we discuss the results of our DEM analysis. We used the DEM distribution for the quiet Sun obtained by Brooks & Warren (2006) using CDS data as an initial estimate for the EIS data. We then modified the shape and magnitude to reproduce as many of the 29 spectral line intensities as possible to within our hoped for tolerance level of 30%.

5.1. Best Case DEM

Figure 3 shows the DEM solution over the temperature interval $\log T_e = 5.4\text{--}6.6$ K. Five of the spline knots used are shown by the boxes on the plot. The other two are positioned at $\log T_e = 4.5$ and 5.05 K, and are outside the temperature range plotted and the temperature range over which the solution is well constrained. The shape of the DEM distribution ended up being remarkably similar to that found in the previous study. As in that study, and Warren (2005), the DEM distribution in the $\log T_e = 5.8\text{--}6.3$ range requires close spacing of the knots to represent the sudden decrease in emission measure that is characteristic of the usual quiet Sun DEM distribution at high temperatures. The lower panel shows ratios of observed to DEM predicted intensities for the lines of Fe, S, and Si used in the analysis: only lines of these atomic species made it into the final set of 29. These ratios are plotted at the temperature of the peak of the relevant contribution function.

Table 1 gives the detailed observed intensities and numbers from the computations. The temperature of peak abundance in ionization equilibrium for each line is also given, though, as already stated, there is evidence that these calculations and therefore the ion formation temperatures, may need revision (Young et al. 2007a). The wavelengths are taken from the literature values of Brown et al. (2008). It has been noted before that there is a difficulty in reproducing both the Fe and Si lines simultaneously with the DEM method. Warren (2005) addressed this issue by increasing the Si abundance by 30% in his analysis, while Brooks & Warren (2006) did the same but also increased the Fe abundance by 10%. Both these analyses point to a 20–30% relative modification of the abundances between Fe and Si. Here we found that a slightly larger relative modification, this time reducing the Fe abundance by $\sim 40\%$, brings the Fe and Si lines into better agreement.

Table 1 shows that the majority of the lines (70%) are reproduced to within $\sim 30\%$ or better, which was our stated goal. Only 8 lines (27%) are reproduced to worse than $\sim 50\%$ and

possible reasons for this are discussed below. Above $\log T_e = 6.1$ K, the distribution is well constrained with 11 of the 13 Fe and Si lines reproduced to within $\sim 30\%$. These results are also comparable to those we obtained in our previous study. There is an interesting contrast with CDS, however, in that the CDS DEM is well constrained in the lower temperature range ($\log T_e = 5.1\text{--}5.7$ K) whereas the EIS DEM is best constrained at higher temperatures (above $\log T_e = 6.1$ K). This is as one would expect given the different target wavelength and temperature regimes of the two instruments, but also indicates that there is greater uncertainty in our understanding of the DEM distribution between $\log T_e = 5.7\text{--}6.1$ K.

Figure 4 shows the Brooks & Warren (2006) DEM (dashed line), and the current DEM derived using EIS data (solid line). The curves are plotted over the same temperature range as in Figure 3. In the lower panel, the ratio of the two DEMs is also shown. The DEM curves remain within 50% of each other until they fall rapidly at high temperatures (above $\log T_e = 6.2$ K). This illustrates the similarity in the shapes of the two DEM curves, despite being derived from different regions using different instrumentation.

5.2. Discrepancies between Observed and Predicted Intensities

The accuracies of the predicted line intensities can be seen in Table 1. The following lines were reproduced to worse than 50% accuracy:

1. The Cl-like Fe X lines at 193.715 \AA , 195.399 \AA , and 257.262 \AA are all observed to be stronger than the DEM predicts by varying factors.

Examining our fit to the 193.715 \AA line in detail we are not convinced that it is perfect because the line blends into the wings of the nearby S X 193.469 \AA line. We find, however, that further attempts to refine our fit lead to an increased measured intensity for the 193.715 \AA line which exacerbates the mismatch problem. We can only reduce the intensity if the line is blended, but there is no obvious candidate. The CHIANTI database gives an Fe X line of uncertain wavelength at 193.663 \AA but it is not expected to contribute significantly to the feature. The NIST database gives a Na VIII line at 193.558 \AA which could conceivably disturb the fit in the region and is formed around $\log T_e = 5.9$ K according to Mazzotta et al. (1998). We are unable to test this hypothesis, however, as there are no suitable atomic data for this line available in the CHIANTI database.

The 257.262 \AA line is only just over the 50% mismatch level so minor blending at the 10–15% level would be enough to bring the prediction into agreement with the observations. The NIST database shows Mg VIII, Al XII, and O III lines in the $257.2\text{--}257.28 \text{ \AA}$ wavelength range but no suitable atomic data are available to test their contributions.

The worst case for Fe X is the 195.399 Å line where the prediction is nearly a factor of three too weak suggesting that this line is blended. There are a series of Fe X lines in the region of the line, but including them in the contribution function and re-computing the DEM leads to a less than 10% modification to the predicted intensity. The NIST database shows an Al VIII line at 195.374 Å and an Fe VII line at 195.391 Å but no suitable atomic data are available to test their contributions. Empirically the Fe VII 195.391 Å line is found to be a factor of two stronger than the nearby Fe VII 196.22 Å line that is unblended (P.R. Young, private communication). Measuring the 196.22 Å line and correcting by a factor of two leads to a contribution to the 195.399 Å intensity of 20–25%, though the line is very weak in our spectrum. This is not sufficient to resolve the discrepancy found from the DEM analysis.

In the absence of further information we are unable to determine the sources of these discrepancies with confidence. The trend for the observed intensities to be larger than the predicted ones may suggest that there are additional unknown blends, or that the lines are simply mis-identified in the spectra because, for example, the wavelengths are assigned to the level transitions incorrectly. There is also always the possibility, however, that the atomic data are not sufficiently accurate.

2. The S-like Fe XI 188.299 Å line is about a factor of two stronger than predicted by the DEM. It is partially blended with the Fe XI 188.216 Å line but both are easily separable when fitted. The 188.299 Å line intensity would need to be blended with an unknown line of comparable strength to account for the discrepancy but there is no obvious candidate line to be the blend. The NIST database shows no Fe XI line at 188.299 Å and Young et al. (2007a) note that the identification of one or both of these lines is uncertain. The line at 188.216 Å is reproduced to high accuracy by the DEM, however, so this identification looks secure. It could be that the transition identification or wavelength for the 188.299 Å line is incorrect in the CHIANTI database. Alternatively, it may just be a mis-identification.

3. The P-like Fe XII line at 256.925 Å is significantly stronger than predicted by the DEM (factor of 25). This large discrepancy points to significant problems with the atomic data for this line or that it is mis-identified.

It has been used on its own here, but the feature also contains weaker contributions from two other lines around 256.94 Å. Even including these lines, however, the prediction is still over an order of magnitude out. One possibility is that there are many more weak contributing lines than expected around this wavelength, perhaps from higher level transitions, but this is purely conjecture. The current results suggest that the collisional or radiative rates for this transition need significant improvement, or that it is mis-identified.

4. The O-like Si VII 275.352 Å line is predicted to be a factor of 2.6 higher than observed and the recently proposed identifications of Ar-like Fe IX lines at 188.485, 189.940, and 197.858 Å are all predicted to be 65–85% brighter than observed. These measurements show a contrasting trend to the cases already discussed i.e. the predicted intensities are greater than the observed ones, and imply that the presence of unknown blends would only increase the discrepancy because the observed intensity would be reduced. Identifying the 189.940 Å feature as a line of Fe XI as in Brown et al. (2008), for example, leads to a computed intensity that is a factor of two too high, even without Fe IX. This in turn suggests that there are problems with the atomic data for these lines, or that the identifications are uncertain.

As mentioned, there is greater uncertainty in the DEM distribution in the temperature range ($\log T_e = 5.7\text{--}6.1$ K) in which these lines are formed. If a local minimum with a reduction in the DEM of about a factor of two is introduced around $\log T_e = 5.8$ K then the Fe IX lines at 188.485 Å and 189.940 Å *can* be reproduced at the expense of losing the agreement for Fe X 190.038 Å and Fe XIV 264.787 Å. Furthermore, if the minimum is accentuated, the Fe IX 197.858 Å line comes into agreement and with a reduction of a factor of four even the Si VII 275.352 Å line can be reproduced at the expense of the Fe VIII lines at 185.213 Å and 186.601 Å. Therefore, of the eight lines discussed, only four of any species or ionization state can be reproduced simultaneously.

We decided to favor the Fe VIII lines in this study for five reasons. First, the solutions including the Fe IX and Si VII lines destroy the agreement found between the current best case EIS DEM distribution and that of our previous study derived from CDS data because of the minimum around $\log T_e = 5.8$ K. There is no evidence for such a deep local minimum in the DEM distribution at these temperatures from previous quiet Sun DEM studies, nor is one expected when one considers the radiative loss curve in this temperature region. Second, recent new ionization fraction calculations by Bryans et al. (2009) indicate that the peak fractional abundance for Fe IX is about 20% too high in the Mazzotta et al. (1998) calculations. A corresponding reduction in our predicted intensities would bring the Fe IX lines to within 30–50% of the observed intensities and therefore into closer agreement with the best case EIS DEM emphasizing Fe VIII. Third, the Bryans et al. (2009) results also indicate that the Si VII peak fractional abundance should be increased by a factor of two. This is much larger than the changes for Fe VIII or Fe IX indicating that the Si VII ionization balance derived by Mazzotta et al. (1998) is considerably uncertain. Fourth, all of the other Si lines used in the study are reproduced satisfactorily without the minimum. Finally, our objective, for this study, is to find a series of reliable Fe lines.

The problems above are also compounded by uncertainty in the formation temperatures of the lines themselves. Young et al. (2007b) used a comparison of coronal loop images

formed from the Si VII 275.352 Å line with images formed from the Fe VIII 185.213 Å line to suggest that Fe VIII was actually formed at a higher temperature ($\log T_e = 5.8$ K) than the Mazzotta et al. (1998) ionization balance calculations would suggest ($\log T_e = 5.6$ K). Their argument was based on the fact that the atomic structure of Fe is more complex than that of Si, but this issue requires further attention because of the potential problem found here with Si VII 275.352 Å. Brown et al. (2008) identify seven Fe VIII lines and five Si VII lines in their EIS quiet Sun spectrum. If the temperature of formation of these lines in ionization equilibrium is the problem they should all be shifted in the same way. An inspection of images in all these lines, or a more quantitative comparison of, e.g., relative intensity profiles with location (Brooks et al. 1999), may firm up conclusions on this issue.

5.3. DEM Subset and Iron Only

We have applied the best case EIS DEM solution for the lines in Table 1 to the complete dataset of 77 fitted spectral lines to obtain a global view of the reliability of the other lines, and to confirm the identification of single reliable lines at each temperature that could be used to derive a DEM curve with minimal measurements. Our expectation, of course, was that many of these lines would come from the set already used for our best case solution except for cases where another line was needed to fill in a temperature interval.

Figure 5 shows the result of that application in the same format as Figure 3. Empty colored circles now indicate lines that were fitted and reproduced by the DEM, but were deselected because a better candidate line existed at the same temperature. Before referring to that discussion, however, note the significant spread in observed to predicted ratios for many of the lines. In many cases, the predicted intensities are factors of two or more out. A possible explanation for these discrepancies is that the lines are weak or blended with unidentified lines. A more detailed analysis of the weaker lines would be needed to confirm or reject this suggestion.

Having commented on that possibility, however, there are many cases where the error in the Gaussian fit is relatively large compared to that of the lines in the initial selection (Table 2), but the fit itself still looks very good. We believe, therefore, that many additional weaker lines in the EIS spectra could be used usefully for future studies. The available atomic data for many lines, however, are not of sufficient accuracy at this stage for that purpose (especially lines of Fe). As pointed out earlier and by others (Lanzafame et al. 2002; Young et al. 2007b) the atomic modeling for complex species such as Fe needs significant improvement, especially for the analysis of weaker low signal-to-noise lines presumably emitted from transitions between higher levels where the population structure needs more detailed modeling.

State-of-the-art solar spectroscopic observations continue to provide useful guidance for the direction of modeling efforts.

The filled circles in Figure 5 now represent the best reliable lines selected at each temperature. In making that choice, stronger lines were preferred over weaker lines (if two lines were reproduced to the same accuracy level) and Fe lines were preferred over other species (in an attempt to provide a subset of Fe lines that could be used to obtain the DEM free of uncertainties in the elemental abundances).

The final subset of selected lines is given in Table 2 and they are mostly strong Fe lines. One Mg and one Al line are also included to fill out the temperature range.

The subset of lines clearly works. It spans the temperature interval $\log T_e = 5.55\text{--}6.35$ K and can reproduce the best case EIS DEM of Figure 4 well with a comparable reduction in the abundance of Fe to that adopted in §5.1. The Al and Mg lines can also be brought into agreement with the others by decreasing their elemental abundances by 20–30%. Since these abundance adjustments are based only on the measurement of one line we consider this solution unsatisfactory. In fact, if we decrease the values of the magnitude of the DEM at each temperature by 40% then all the lines can be reproduced to within 20% without the need for adjusting any elemental abundances. This is within the stated accuracy of the EIS photometric calibration measured in the laboratory pre-launch (Lang et al. 2006).

Since many of the selected lines reproduced accurately in this study and shown in Tables 1 and 2 span both the short and long wavelengths of both EIS CCDs A and B, the accuracy of their reproduction essentially provides a preliminary validation of the EIS photometric calibration on orbit. More work and detailed analysis across the complete wavelength range is needed, however.

5.4. Single Pixel DEM

In the previous section we derived the average DEM distribution for this region using a subset of Fe, Mg, and Al lines (see Table 2). Here we use only the subset of Fe lines to demonstrate the sensitivity of EIS by deriving the same DEM distribution from a single EIS pixel. To do so, we applied the average DEM solution to the intensity measurements from the single pixel (marked with small boxes on the images in Figure 2). The Fe abundance was also increased by 10%.

Figure 6 shows the resulting DEM distribution as a function of temperature. The square boxes show the positions of the spline knots used to represent the DEM. The red

dots show the ratios of the observed to predicted intensities scaled by the value of the DEM at the formation temperature of the line. As before, the closer these lines are to the DEM curve the better they are reproduced. The quantitative values from the analysis are given in Table 3, which is in the same format as Tables 1 and 2. It can be seen that each of the dots lies nicely on the curve. The uncertainties in the fits to the line intensities are generally increased compared to the spectrum averaged over the full FOV, being factors of approximately 2–3 larger, though they are still close to our tolerance of about 30% except for the low signal-to-noise Fe XV 284.160 Å line. The uncertainty in the fitted intensity of the latter line becomes comparable to that for Fe XIV 274.203 Å if we average the spectrum over 2–4 pixels (depending on the quality of the spectra).

The Fe lines span the temperature interval $\log T_e = 5.55\text{--}6.35$ K and they are all reproduced to within 16%. This result demonstrates the aptitude of EIS for studies of inhomogeneities in the DEM distribution at high spatial resolution.

5.5. Single Pixel DEM with MCMC algorithm

As an independent verification of the results we also applied a Monte Carlo Markov Chain (MCMC) emission measure algorithm (Kashyap & Drake 1998) to the data. The code is available in the PINTofALE IDL analysis package (Kashyap & Drake 2000). The derived DEM distribution is shown in Figure 7 (histogram plot), together with the DEM loci curves derived from the results for each spectral line using the formulation

$$EM(T_e) = I_{nl}/(G(T_e, N_0) \times T_e) \quad (2)$$

Here, N_0 is the measured value of electron density for this dataset. The MCMC DEM results were used to predict the spectral line intensities and the results are given in the final two columns of Table 3. These are very close to the results obtained using the spline method, except for Fe XIV 274.203 Å which is about 60% too low. This difference could indicate that the emission measure should be increased at the formation temperature of Fe XIV, which could be evidence of a high temperature tail in the DEM distribution. This possibility is discussed in detail in Warren & Brooks (2009).

6. Uniformity of the quiet Sun DEM distribution

An immediate advantage of obtaining a reliable subset of Fe lines is that we can assess the generality of our results quickly. We compared the averaged intensities for the Fe lines recommended in the final subset over a 20 hour period surrounding the main observations

used in this paper on 2007 January 30–31. All the data were taken using the same EIS study as analyzed here. The observations were also taken with a fixed pointing, so the observed area shifted significantly during this time. We found that the intensities of these Fe lines varied by less than 18% between the datasets and that they can therefore be reproduced with the same DEM curve as derived for the main dataset.

To explore the uniformity of the quiet Sun DEM distribution in general, we collected 39 additional datasets taken between 2007 January 25 and April 14. These latter datasets were obtained with a different observing sequence with study acronym SYNOP001. This study takes two 40" slot images followed by two 1" slit exposures with times of 30s and 90s, respectively. It also returns full CCD spectra, but the FOV is only 1" × 256" (for the slit exposures). Here we used the 90s exposure from each dataset and averaged the spectra over the full 256" slit direction.

SYNOP001 is nominally run on quiet Sun near disk center to monitor the EIS sensitivity. In the early stages of the mission, however, it was also used to obtain full CCD spectra of other targets. By checking EIT and *Hinode* X-ray Telescope (XRT, Golub et al. 2007) full Sun images from 2007 January to April, we were able to select time periods when solar disk center was free of any influence from active regions or equatorial coronal holes. The 39 datasets represent the result of that verification after also ignoring observations that were pointed far from disk center. We then reduced the datasets as before and fitted the subset of Fe lines in order to perform a DEM analysis on all 45 datasets. The results are shown in Table 4.

Table 4 gives the date and start time of the observations in columns 2 and 3. The HPW001_FULLCCD_RAST datasets are numbered 10–15 in column 1. All the other datasets are from SYNOP001 observations. Our goal was to check if the shape of the DEM distribution changed significantly from quiet Sun region to region. So we initially applied our best-case solution to the averaged spectrum of each dataset to see whether the observed line intensities could be reproduced. If not, we then adjusted the DEM curve. Since the shape of the DEM is the key point of interest here, we scaled the DEM by an adjustable constant factor to try to match the intensities. We only modified the shape if it became necessary. This constant factor (α) is given in column 4 of the table and varies by up to a factor of 2 in the regions we have analyzed. This factor is a measure of the relative difference between the DEM curves on an absolute magnitude scale and may be representative of the amount of heating in each region. Alternatively, it could indicate a deviation from the adopted Fe abundance (in fact α was derived by adjusting this abundance). A mean dataset created by averaging all the intensities in each column (i.e. averaging over all the datasets) is also added in the last row of the table.

Columns 6–12 give the observed intensities of the 7 Fe lines from the subset, and in brackets we show the ratios of predicted to observed intensities from the DEM solutions we derived. The measurement uncertainties from the spectral fits are not shown to preserve table space. Of the 315 intensities shown in the table only 3 are reproduced to worse than 30%. All 3 cases are Fe XIV 274.203 Å intensities and in all 3 cases the predicted intensity is too low. These cases behave like the MCMC solution presented in §5.5 and may be further evidence of a high temperature tail in the distribution. It is also possible, however, to modify the high temperature distribution to reproduce this intensity at the expense of other lines.

Figure 8 shows a plot of all the DEM solutions derived from all of the datasets listed in Table 4. This figure clearly illustrates the similarity in the shapes of the curves. In §5.1 we showed that the Brooks & Warren (2006) and EIS DEMs maintained similar shapes up to $\log T_e = 6.2$ K when the lines become weak and the curves start to fall rapidly. Figure 8 demonstrates that this is true in general. All the curves maintain similar shapes up to at least $\log T_e = 6.1$.

We calculated ratios of each DEM solution to the distribution derived from the January 30 11:19UT dataset as a function of temperature and measured the temperature at which the ratio for each curve deviated by more than 50%. These values are given in column 5 of Table 4. The vast majority (93%) of the curves do not deviate by more than 50% until $\log T_e = 6.15$ K, and two thirds of the curves are within this limit until $\log T_e = 6.2$ K. Note that in many cases the January 30 distribution is able to reproduce all of the intensities. The eye is naturally drawn to the spread in the curves at high temperature in Figure 8, but a value of 6.8 in the Table indicates that the curve never deviates by more than 50%.

7. Summary and Discussion

We have performed a DEM analysis of a quiet coronal region using observations obtained by *Hinode*/EIS. We find that the well-known quiet coronal DEM distribution can be recovered as expected, and that the intensities of the majority of the reliable lines, averaged over the full FOV, can be reproduced to within 30%. Only about one quarter of the spectral line intensities are reproduced to worse accuracy than 50%, and this result is comparable to that achieved for previous EUV spectrometers, for example, CDS (Brooks & Warren 2006).

The analysis also provides clues to the explanations for the discrepancies found for some lines that could be exploited in the future. Despite recent improvements in the fundamental atomic data available for Fe XII, for example, problems remain for some lines (e.g., Fe XII 256.925 Å). As suggested by previous authors (Lanzafame et al. 2002; Young et al. 2009),

further improvement in the atomic modeling of complex species such as Fe is necessary to fully exploit the high quality EIS observations.

We present also a subset of nine EIS lines spanning the temperature interval $\log T_e = 5.55\text{--}6.35$ K that can be used to derive the DEM distribution reliably. This includes a series of seven Iron lines that can be used to derive the DEM distribution free from the possibility of uncertainties in the elemental abundances. This subset is likely to be useful for extensive studies of, e.g., the temporal evolution of the DEM during active events.

We have also demonstrated the power of EIS for studies of spatial inhomogeneities in the quiet coronal DEM distribution by deriving the DEM curve from a single EIS pixel. The curve was shown to follow the same shape as the DEM curve derived from a spectrum produced by averaging the whole observed field-of-view. All of the observed intensities from a subset of Fe lines are reproduced to within 16%. This is in fact better than the result obtained for the averaged spectrum, though the fitted intensities have larger uncertainties.

Since many of the lines in Tables 1 and 2 are reproduced to within the accuracy of the pre-launch laboratory calibration of EIS and span both the short and long wavelength ranges of both CCDs, this analysis also provides a preliminary validation of the photometric calibration of EIS on orbit, that was realized to unprecedented accuracy in the laboratory. Thus the pre-launch calibration can be used with confidence. Regular observations are carried out by the EIS team to monitor any degradation in sensitivity with time.

The EIS DEM is very similar to that derived in Brooks & Warren (2006) using CDS data. They were derived independently from data taken nearly 9 years apart, using completely different spectral lines, in completely different EUV wavelength ranges, with their own associated atomic data uncertainties and instrument specific issues, yet the two curves maintain basically the same shape in the temperature interval $\log T_e = 5.4\text{--}6.2$ K. We confirmed that this result was true in general by analyzing 45 EIS quiet Sun datasets taken in the period 2007 January to April.

Attempts to use the DEM to infer information about the heating have a long history, see e.g. Jordan (1980), and it is well known that hydrostatic simulations of uniformly heated coronal loops fail to correctly model the DEM distribution (Schrijver & Aschwanden 2002, and references therein). In particular, the slope of the DEM below the peak is much steeper in the observations. Using loops with expanding cross-section, or incorporating loop foot-point heating, improves the agreement but does not solve the problem. Hydrodynamic modeling may provide further insight, but introduces flows that are assumed to be negligible in the DEM method. Nevertheless, the observation of a *universal* DEM throughout the quiet Sun (even down to small spatial scales) is potentially an important result because it provides a

further constraint on the heating mechanism.

The shape of the DEM as a function of temperature is dependent on several terms in the energy balance equation, and the relative importance of flows, loop geometry, the heating mechanism, and cooling by radiation and conduction is not known. One possibility is that although the absolute magnitude of the quiet Sun DEM may scale with the amount of energy released in each region, the *shape* of the distribution is mainly a function of the radiating and conducting properties of the plasma, and is fairly insensitive to the location and rate of energy deposition. Since these functions have a fixed shape, the DEM would also have a fixed shape if they dominate the energy balance. The loop geometry and the heating mechanism could, in principle, vary from location to location, but if they are the dominant factors controlling the DEM shape then the observation that the DEM does not vary would imply that these factors also do not vary substantially from region to region. We expect that there are several heating mechanisms operating in the quiet Sun, so these observations imply either that one is dominant, or that their influence on the DEM shape is negligible.

We thank John Mariska and Peter Young for helpful comments and suggestions. We also thank the referee for constructive suggestions on how to physically interpret the results. DHB and HPW acknowledge funding support from the NASA Hinode program. CHIANTI is a collaborative project involving the NRL (USA), RAL (UK), and the following Universities: College London (UK), Cambridge (UK), George Mason (USA), and Florence (Italy). *Hinode* is a Japanese mission developed and launched by ISAS/JAXA, with NAOJ as domestic partner and NASA and STFC (UK) as international partners. It is operated by these agencies in co-operation with ESA and NSC (Norway).

Facilities: Hinode (EIS), SOHO (EIT)

REFERENCES

- Aschwanden, M. J., Alexander, D., Hurlburt, N., Newmark, J. S., Neupert, W. M., Klimchuk, J. A., & Gary, G. A. 2000, ApJ, 531, 1129
- Aschwanden, M. J., Newmark, J. S., Delaboudinière, J.-P., Neupert, W. M., Klimchuk, J. A., Gary, G. A., Portier-Fozzani, F., & Zucker, A. 1999, ApJ, 515, 842
- Brooks, D. H., et al. 1999, A&A, 347, 277
- Brooks, D. H., & Warren, H. P. 2006, ApJS, 164, 202

- Brosius, J. W., Davila, J. M., Thomas, R. J., & Monsignori-Fossi, B. C. 1996, *ApJS*, 106, 143
- Brown, C. M., Feldman, U., Seely, J. F., Korendyke, C. M., & Hara, H. 2008, *ApJS*, 176, 511
- Bryans, P., Landi, E., & Savin, D. W. 2009, *ApJ*, 691, 1540
- Culhane, J. L., et al. 2007, *Sol. Phys.*, 243, 19
- Del Zanna, G., & Mason, H. E. 2005, *A&A*, 433, 731
- Dere, K. P., Landi, E., Mason, H. E., Monsignori Fossi, B. C., & Young, P. R. 1997, *A&AS*, 125, 149
- Domingo, V., Fleck, B., & Poland, A. I. 1995, *Sol. Phys.*, 162, 1
- Feldman, U., Mandelbaum, P., Seely, J. F., Doschek, G. A., & Gursky, H. 1992, *ApJS*, 81, 387
- Golub, L., et al. 2007, *Sol. Phys.*, 243, 63
- Harrison, R. A., et al. 1995, *Sol. Phys.*, 162, 233
- Jordan, C. 1980, *A&A*, 86, 355
- Kashyap, V., & Drake, J. J. 1998, *ApJ*, 503, 450
- Kashyap, V., & Drake, J. J. 2000, *Bulletin of the Astronomical Society of India*, 28, 475
- Kosugi, T., et al. 2007, *Sol. Phys.*, 243, 3
- Landi, E., Del Zanna, G., Young, P. R., Dere, K. P., Mason, H. E., & Landini, M. 2006, *ApJS*, 162, 261
- Lang, J., et al. 2006, *Appl. Opt.*, 45, 8689
- Lanzafame, A. C., Brooks, D. H., & Lang, J. 2005, *A&A*, 432, 1063
- Lanzafame, A. C., Brooks, D. H., Lang, J., Summers, H. P., Thomas, R. J., & Thompson, A. M. 2002, *A&A*, 384, 242
- Lenz, D. D., Deluca, E. E., Golub, L., Rosner, R., & Bookbinder, J. A. 1999, *ApJ*, 517, L155
- Markwardt, C. B. 2009, *ArXiv e-prints*

- Mazzotta, P., Mazzitelli, G., Colafrancesco, S., & Vittorio, N. 1998, *A&AS*, 133, 403
- Schmelz, J. T., Scopes, R. T., Cirtain, J. W., Winter, H. D., & Allen, J. D. 2001, *ApJ*, 556, 896
- Schrijver, C. J., & Aschwanden, M. J. 2002, *ApJ*, 566, 1147
- Summers, H. P., et al. 2006, *Plasma Physics and Controlled Fusion*, 48, 263
- Warren, H. P. 2005, *ApJS*, 157, 147
- Warren, H. P., & Brooks, D. H. 2009, *ApJ*, 700, 762
- Warren, H. P., Ugarte-Urra, I., Doschek, G. A., Brooks, D. H., & Williams, D. R. 2008, *ApJ*, 686, L131
- Watanabe, T., Hara, H., Culhane, L., Harra, L. K., Doschek, G. A., Mariska, J. T., & Young, A. R. 2007, *PASJ*, 59, 669
- Young, P. R. 2005, *A&A*, 439, 361
- Young, P. R. 2009, *ApJ*, 691, L77
- Young, P. R., et al. 2007a, *PASJ*, 59, 857
- Young, P. R., Del Zanna, G., Mason, H. E., Doschek, G. A., Culhane, L., & Hara, H. 2007b, *PASJ*, 59, 727
- Young, P. R., Watanabe, T., Hara, H., & Mariska, J. T. 2009, *A&A*, 495, 587

Table 1. Quiet Sun intensities from the EIS Spectrometer.

Ion	λ_{obs} (Å)	$\log T_{max}$ (K)	I_{obs}^a	I_{dem}^a	Ratio
FE VIII	185.213	5.55	19.73±0.06	20.81	1.05
FE VIII	186.601	5.55	14.77±0.05	14.60	0.99
Si VII	275.352	5.70	10.52±0.04	27.08	2.57
FE IX	188.485	5.80	14.13±0.03	23.27	1.65
FE IX	189.940	5.80	8.24±0.05	13.42	1.63
FE IX	197.858	5.80	8.78±0.03	16.06	1.83
FE X	177.239	6.00	109.74±0.52	140.64	1.28
FE X	184.537	6.00	57.21±0.09	55.72	0.97
FE X	190.038	6.00	20.34±0.07	15.67	0.77
FE X	193.715	6.00	4.72±0.02	2.79	0.59
FE X	195.399	6.00	4.35±0.03	1.48	0.34
FE X	257.262	6.00	47.66±0.08	31.11	0.65
FE XI	180.401	6.05	190.56±0.30	185.56	0.97
FE XI	182.167	6.05	21.95±0.11	24.85	1.13
FE XI	188.216	6.05	93.95±0.10	87.57	0.93
FE XI	188.299	6.05	64.03±0.10	31.88	0.50
S X	264.233	6.10	14.26±0.05	11.35	0.80
FE XII	192.394	6.15	36.96±0.04	48.48	1.31
FE XII	193.509	6.15	79.57±0.06	102.19	1.28
FE XII	195.119	6.15	135.38±0.05	151.45	1.12
FE XII	256.925	6.15	13.62±0.06	0.68	0.05
Si X	258.375	6.15	31.84±0.07	28.12	0.88
Si X	261.058	6.15	16.61±0.05	16.49	0.99
Si X	271.990	6.15	15.57±0.05	12.39	0.80
Si X	277.255	6.15	10.06±0.05	10.14	1.01
FE XIII	202.044	6.20	82.05±0.09	80.63	0.98
FE XIV	264.787	6.25	9.43±0.05	7.23	0.77
FE XIV	274.203	6.25	11.26±0.05	10.76	0.96
FE XV	284.160	6.35	13.16±0.08	15.18	1.15

^aUnits are $\text{erg cm}^{-2} \text{s}^{-1} \text{sr}^{-1}$.

Table 2. Quiet Sun intensities from the EIS Spectrometer.

Ion	λ_{obs} (Å)	$\log T_{max}$ (K)	I_{obs}^a	I_{dem}^a	Ratio
FE VIII	185.213	5.55	19.73±0.06	18.44	0.93
Mg VI	268.986	5.60	2.72±0.08	2.50	0.92
FE X	184.537	6.00	57.21±0.09	49.38	0.86
FE XI	188.216	6.05	93.95±0.10	77.61	0.83
Al IX	284.015	6.05	2.89±0.09	3.36	1.16
FE XII	195.119	6.15	135.38±0.05	134.23	0.99
FE XIII	202.044	6.20	82.05±0.09	71.47	0.87
FE XIV	274.203	6.25	11.26±0.05	9.54	0.85
FE XV	284.160	6.35	13.16±0.08	13.46	1.02

^aUnits are $\text{erg cm}^{-2} \text{s}^{-1} \text{sr}^{-1}$.

Table 3. Quiet Sun intensities from a single EIS pixel.

Ion	λ_{obs} (Å)	$\log T_{max}$ (K)	I_{obs}^a	I_{dem}^a	Ratio	I_{dem}^b	Ratio ^b
Fe VIII	185.213	5.55	18.63±5.40	20.26	1.09	18.98	1.02
Fe X	184.536	6.00	58.01±11.02	54.27	0.94	65.05	1.12
Fe XI	188.216	6.05	99.04±9.90	85.29	0.86	92.23	0.93
Fe XII	195.119	6.15	129.65±6.48	147.50	1.14	128.06	0.99
Fe XIII	202.044	6.20	80.11±10.41	78.53	0.98	88.40	1.10
Fe XIV	274.203	6.25	12.03±4.09	10.48	0.87	7.37	0.61
Fe XV	284.160	6.35	13.65±7.64	14.79	1.08	15.33	1.12

^aUnits are $\text{erg cm}^{-2} \text{s}^{-1} \text{sr}^{-1}$.

^bResults using MCMC algorithm.

Table 4. Quiet Sun intensities from 45 datasets.

No.	Date	Time ^b	α^d	T_{cut}^e	$I_{obs}^a (I_{dem}/I_{obs})$						
					Fe VIII	Fe X	Fe XI	Fe XII	Fe XIII	Fe XIV	Fe XV
					185.213 λ	184.536 λ	188.216 λ	195.119 λ	202.044 λ	274.203 λ	284.160 λ
1	25-Jan-07	17:51:36	1.5	6.80	21.01 (1.28)	58.91 (1.23)	96.19 (1.18)	193.38 (1.01)	131.29 (0.80)	17.78 (0.78)	23.43 (0.84)
2	26-Jan-07	00:06:50	1.0	6.80	17.58 (1.05)	48.36 (1.02)	74.22 (1.05)	115.91 (1.16)	66.73 (1.07)	11.39 (0.84)	14.25 (0.94)
3	26-Jan-07	06:04:49	1.1	6.25	15.37 (1.27)	44.67 (1.22)	84.97 (1.03)	140.94 (1.11)	79.65 (1.11)	16.10 (0.79)	19.21 (1.05)
4	26-Jan-07	12:09:28	0.8	6.80	18.24 (0.79)	43.65 (0.89)	70.09 (0.87)	104.28 (1.01)	62.76 (0.89)	8.42 (0.89)	8.29 (1.27)
5	26-Jan-07	18:09:50	0.8	6.80	19.82 (0.77)	49.92 (0.82)	76.99 (0.84)	110.17 (1.01)	56.40 (1.05)	8.56 (0.93)	8.60 (1.30)
6	27-Jan-07	06:28:49	0.9	6.40	21.60 (0.77)	53.65 (0.83)	90.47 (0.77)	107.10 (1.11)	50.77 (1.22)	8.06 (1.00)	8.35 (1.30)
7	27-Jan-07	11:59:28	0.7	6.30	17.61 (0.78)	43.97 (0.84)	74.47 (0.78)	101.45 (0.97)	52.02 (0.97)	7.57 (0.84)	6.47 (1.27)
8	28-Jan-07	00:02:50	1.2	6.10	29.91 (0.81)	74.39 (0.77)	80.11 (0.97)	85.14 (1.29)	33.67 (1.30)	5.65 (0.68)	3.38 (0.93)
9	28-Jan-07	06:02:49	1.1	6.10	23.54 (0.88)	63.13 (0.77)	71.74 (0.85)	62.62 (1.23)	20.20 (1.31)	2.99 (0.59)	1.16 (0.77)
10	30-Jan-07	11:19:12	1.1	6.80	19.15 (1.04)	54.69 (0.98)	94.47 (0.89)	140.57 (1.03)	84.21 (0.92)	11.15 (0.93)	12.74 (1.14)
11	30-Jan-07	14:34:40	1.1	6.80	19.85 (1.03)	57.51 (0.95)	94.86 (0.91)	138.28 (1.08)	82.98 (0.95)	11.27 (0.94)	13.63 (1.09)
12	30-Jan-07	17:50:08	1.0	6.80	19.66 (0.94)	54.67 (0.91)	85.31 (0.91)	122.89 (1.09)	74.59 (0.96)	10.50 (0.91)	13.90 (0.97)
13	30-Jan-07	21:05:35	1.0	6.80	18.52 (1.00)	52.60 (0.94)	83.26 (0.93)	129.61 (1.04)	78.02 (0.92)	9.67 (0.99)	12.54 (1.07)
14	31-Jan-07	00:21:02	1.1	6.80	18.83 (1.11)	56.82 (0.98)	97.46 (0.90)	145.76 (1.04)	87.77 (0.92)	11.66 (0.92)	15.26 (1.00)
15	31-Jan-07	03:36:29	1.2	6.80	19.05 (1.16)	62.54 (0.95)	108.96 (0.85)	162.39 (0.99)	94.58 (0.91)	11.73 (0.97)	14.55 (1.11)
16	31-Jan-07	12:01:59	1.5	6.80	25.63 (1.08)	80.04 (0.92)	123.75 (0.94)	188.82 (1.06)	110.54 (0.97)	15.07 (0.95)	19.89 (1.01)
17	15-Mar-07	11:19:49	1.2	6.15	20.47 (1.11)	68.23 (0.84)	103.42 (0.79)	131.85 (0.93)	57.47 (0.88)	5.41 (0.82)	2.67 (1.28)
18	15-Mar-07	23:57:28	1.4	6.15	21.45 (1.23)	77.09 (0.86)	119.62 (0.80)	163.32 (0.89)	75.03 (0.82)	7.22 (0.77)	3.44 (1.30)
19	16-Mar-07	11:09:28	1.4	6.15	21.89 (1.21)	77.33 (0.88)	120.65 (0.82)	174.45 (0.87)	80.13 (0.80)	7.82 (0.74)	3.59 (1.29)
20	16-Mar-07	18:01:27	1.5	6.15	25.29 (1.13)	79.02 (0.90)	102.96 (0.97)	126.88 (1.14)	57.30 (1.00)	6.31 (0.72)	2.32 (1.28)
21	17-Mar-07	06:07:27	1.8	6.30	26.30 (1.26)	96.63 (0.91)	168.65 (0.81)	250.97 (0.92)	122.29 (0.97)	17.13 (0.87)	15.22 (1.28)
22	17-Mar-07	09:51:43	1.3	6.35	14.78 (1.28)	62.52 (1.05)	137.71 (0.81)	235.86 (0.84)	136.43 (0.77)	16.67 (0.82)	14.28 (1.25)
23	17-Mar-07	18:03:47	1.5	6.80	17.64 (1.29)	63.94 (1.12)	122.23 (0.94)	209.65 (0.95)	130.62 (0.81)	17.77 (0.80)	18.96 (1.05)
24	18-Mar-07	10:05:53	1.0	6.20	17.85 (1.04)	56.69 (0.86)	89.93 (0.82)	132.11 (0.91)	73.71 (0.79)	8.14 (0.82)	5.94 (1.28)
25	19-Mar-07	11:20:29	1.8	6.20	20.01 (1.26)	68.41 (1.27)	130.33 (1.16)	254.94 (1.16)	211.88 (0.90)	42.41 (0.79)	78.82 (0.91)
26	19-Mar-07	18:06:29	1.2	6.15	16.67 (1.28)	52.31 (1.19)	101.49 (1.08)	231.45 (0.99)	217.55 (0.77)	43.39 (0.80)	91.73 (1.04)
27	20-Mar-07	00:12:51	1.4	6.15	19.20 (1.30)	65.59 (1.14)	116.38 (1.13)	243.21 (1.10)	216.55 (0.83)	42.65 (0.77)	84.74 (0.86)
28	20-Mar-07	06:13:28	1.4	6.15	19.53 (1.28)	70.57 (1.02)	136.74 (0.91)	264.89 (0.96)	215.37 (0.82)	43.86 (0.78)	94.06 (0.90)
29	22-Mar-07	12:55:59	1.5	6.30	22.99 (1.17)	71.71 (1.00)	114.29 (0.98)	164.63 (1.18)	81.25 (1.30)	17.90 (0.83)	29.64 (0.77)
30	23-Mar-07	00:04:50	1.0	6.20	22.97 (0.81)	53.23 (0.91)	79.47 (0.92)	111.87 (1.07)	59.19 (0.97)	8.10 (0.80)	5.62 (1.29)

Table 4—Continued

No.	Date	Time ^b	α^d	T _{cut} ^e	I _{obs} ^a (I _{dem} /I _{obs})						
					Fe VIII	Fe X	Fe XI	Fe XII	Fe XIII	Fe XIV	Fe XV
					185.213 λ	184.536 λ	188.216 λ	195.119 λ	202.044 λ	274.203 λ	284.160 λ
31	23-Mar-07	06:17:58	1.2	6.20	23.50 (0.94)	66.33 (0.87)	113.32 (0.78)	145.81 (0.99)	65.17 (1.09)	10.17 (0.82)	7.56 (1.28)
32	23-Mar-07	06:26:50	1.2	6.25	18.39 (1.21)	61.21 (0.96)	108.83 (0.83)	167.49 (0.90)	93.18 (0.82)	12.24 (0.77)	9.04 (1.30)
33	23-Mar-07	11:55:20	1.1	6.80	16.95 (1.25)	54.17 (1.04)	97.35 (0.91)	157.30 (0.98)	95.38 (0.86)	13.38 (0.82)	13.18 (1.17)
34	23-Mar-07	18:15:20	1.6	6.15	21.03 (1.28)	86.95 (0.89)	150.18 (0.78)	211.77 (0.88)	98.73 (0.87)	11.13 (0.81)	7.03 (1.29)
35	25-Mar-07	00:04:05	1.5	6.80	21.15 (1.30)	82.28 (0.90)	135.97 (0.86)	193.44 (1.04)	103.56 (1.04)	17.75 (0.81)	26.44 (0.77)
36	25-Mar-07	10:45:49	1.3	6.15	25.40 (0.90)	82.74 (0.78)	119.75 (0.80)	151.10 (0.98)	65.12 (1.01)	8.09 (0.82)	5.01 (1.30)
37	25-Mar-07	18:06:19	1.3	6.20	19.13 (1.26)	78.39 (0.80)	114.16 (0.83)	138.90 (1.10)	65.59 (1.10)	7.52 (1.07)	6.88 (1.28)
38	04-Apr-07	05:37:19	1.8	6.80	25.85 (1.28)	85.28 (1.04)	150.05 (0.93)	245.04 (0.98)	148.01 (0.87)	19.22 (0.89)	21.91 (1.10)
39	09-Apr-07	23:57:08	1.5	6.80	20.69 (1.30)	64.73 (1.12)	110.00 (1.04)	194.13 (1.03)	135.27 (0.79)	18.83 (0.77)	19.99 (1.06)
40	10-Apr-07	06:12:49	1.3	6.15	15.14 (1.29)	64.70 (1.06)	142.88 (0.83)	254.14 (0.89)	168.95 (0.79)	25.65 (0.77)	32.57 (0.95)
41	11-Apr-07	13:23:38	1.4	6.15	26.37 (1.01)	77.26 (0.84)	100.50 (0.89)	105.97 (1.19)	37.56 (1.28)	4.17 (0.87)	1.84 (1.19)
42	12-Apr-07	07:30:30	2.0	6.10	43.51 (0.92)	108.17 (0.78)	118.91 (0.89)	122.53 (1.12)	41.64 (1.30)	9.21 (0.57)	5.34 (1.02)
43	12-Apr-07	10:31:50	1.1	6.15	20.06 (0.92)	68.77 (0.80)	102.29 (0.78)	116.80 (0.99)	45.85 (1.02)	5.21 (0.78)	2.58 (1.21)
44	14-Apr-07	13:52:01	1.1	6.30	22.01 (0.92)	64.60 (0.84)	96.85 (0.87)	134.60 (1.06)	62.22 (1.18)	9.45 (0.99)	9.62 (1.27)
45	14-Apr-07	23:43:23	1.5	6.20	21.74 (1.26)	77.65 (0.96)	137.29 (0.88)	232.24 (0.94)	162.83 (0.77)	23.37 (0.80)	27.34 (1.15)
-	Average	-	1.3	6.80	21.18 (1.15)	66.09 (0.99)	107.77 (0.95)	162.59 (1.09)	95.33 (0.99)	14.39 (0.87)	18.68 (0.95)

^aUnits are erg cm⁻² s⁻¹ sr⁻¹.

^bStart time of the first exposure in the raster.

^cUnits are arcsec.

^dScaling factor for the Fe abundance (see text).

^eTemperature at which the DEM deviates from the best-case by more than 50%.

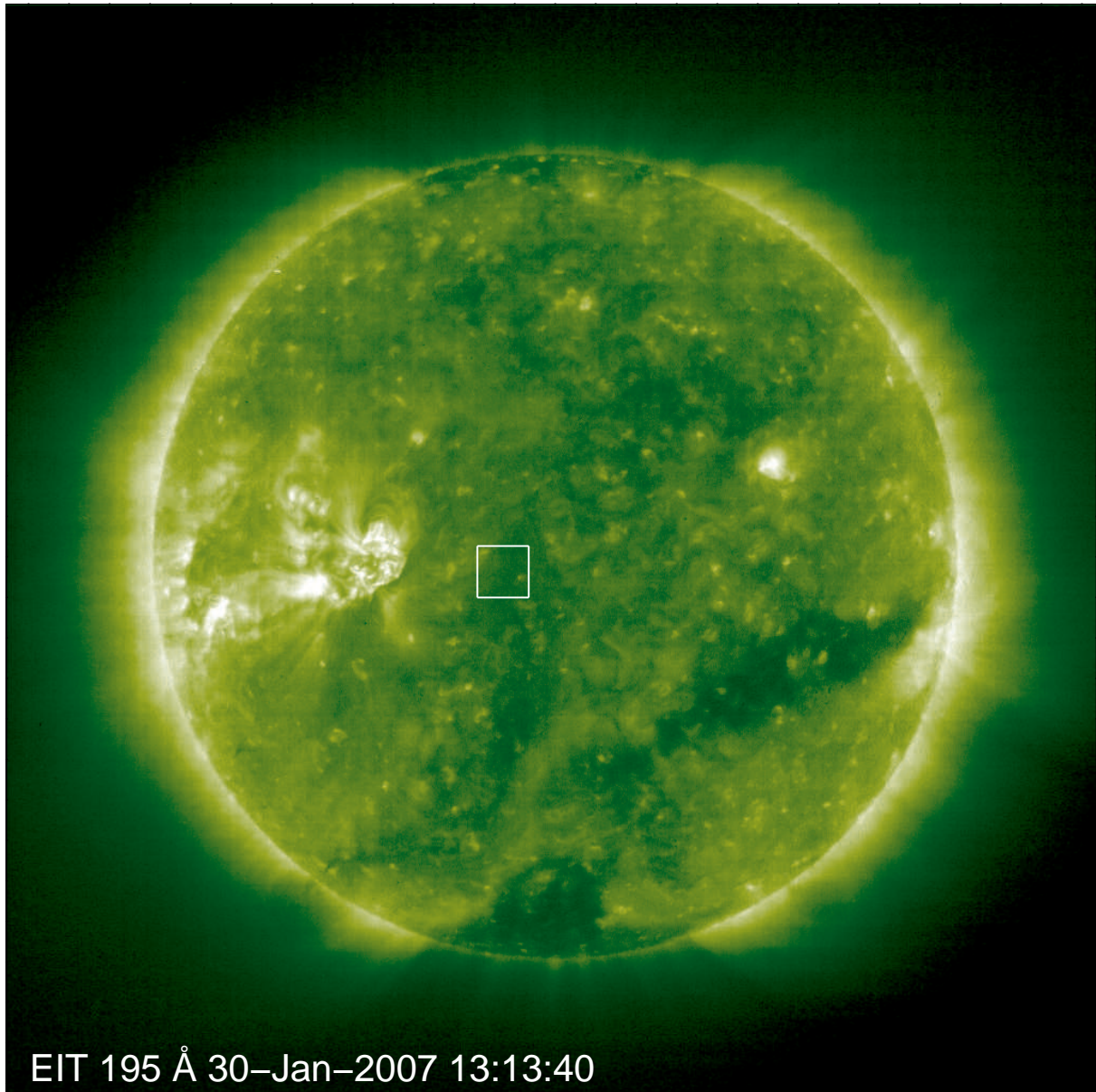


Fig. 1.— Full-disk EIT 195 Å image showing the field-of-view of the EIS study analyzed.

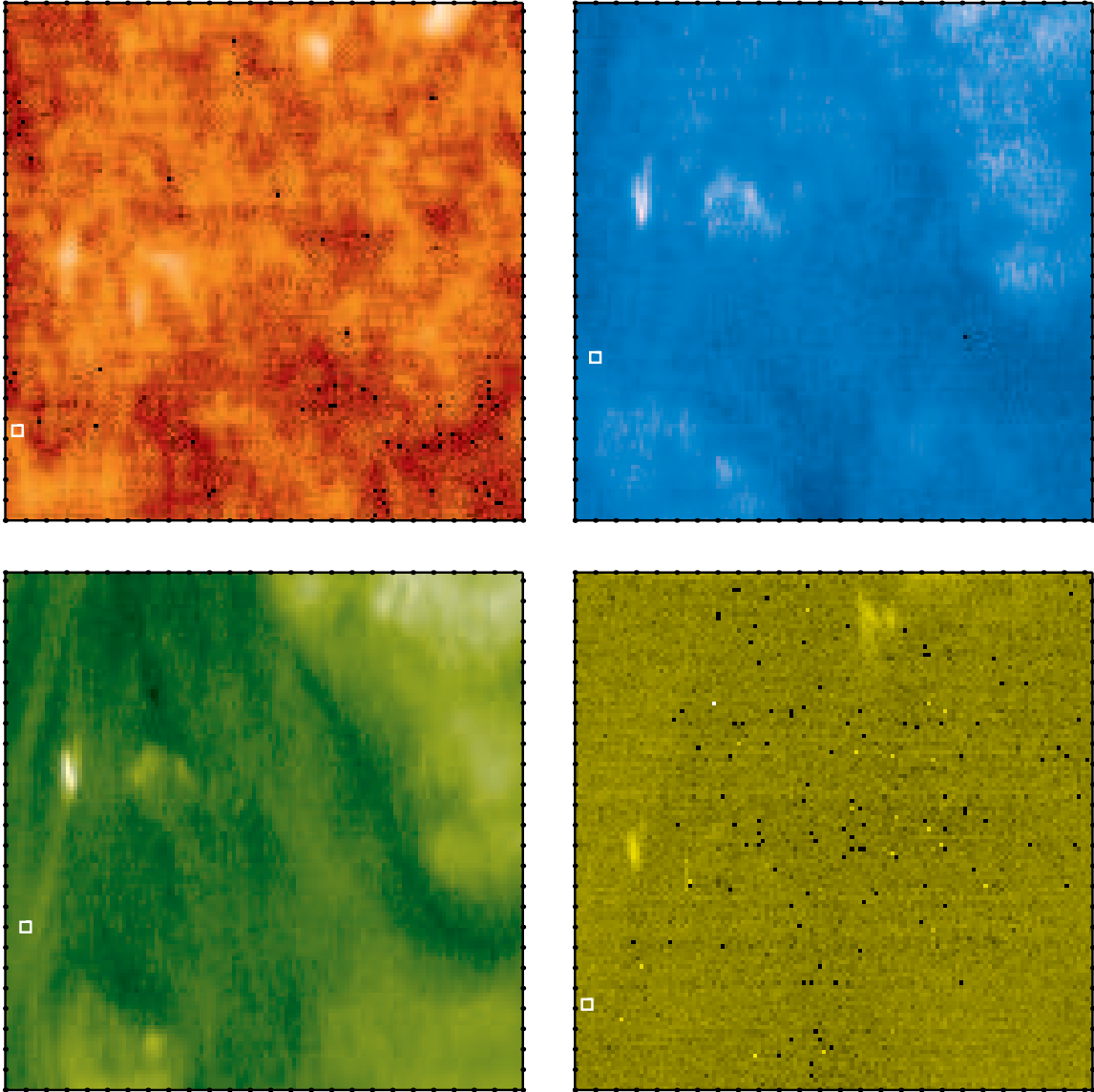


Fig. 2.— EIS images of the observed quiet Sun region. Top Left: Si VII 275.352 Å. Top Right: Fe X 184.537 Å. Bottom Left: Fe XII 195.119 Å. Bottom Right: Fe XV 284.160 Å. The single pixel used in §5.4 is shown as a small (not to scale) box on each image.

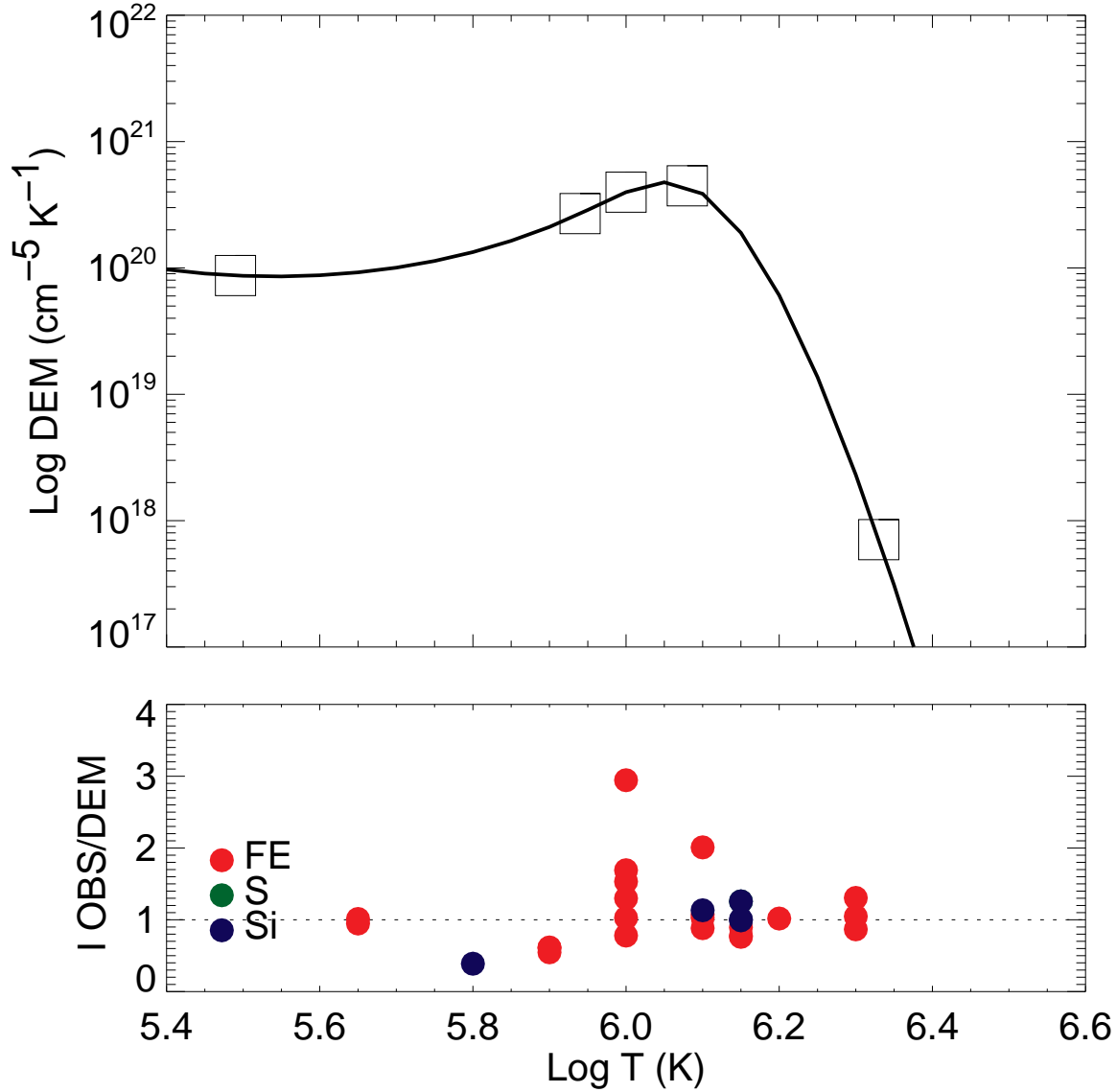


Fig. 3.— The best case DEM solution for the spectral lines shown in Table 1 plotted as a function of temperature (upper panel). The squares show the positions of the spline knots. The lower panel shows ratios of the observed to DEM predicted intensities. The coronal abundance of Feldman et al. (1992) for Fe has been reduced by $\sim 40\%$ for this calculation.

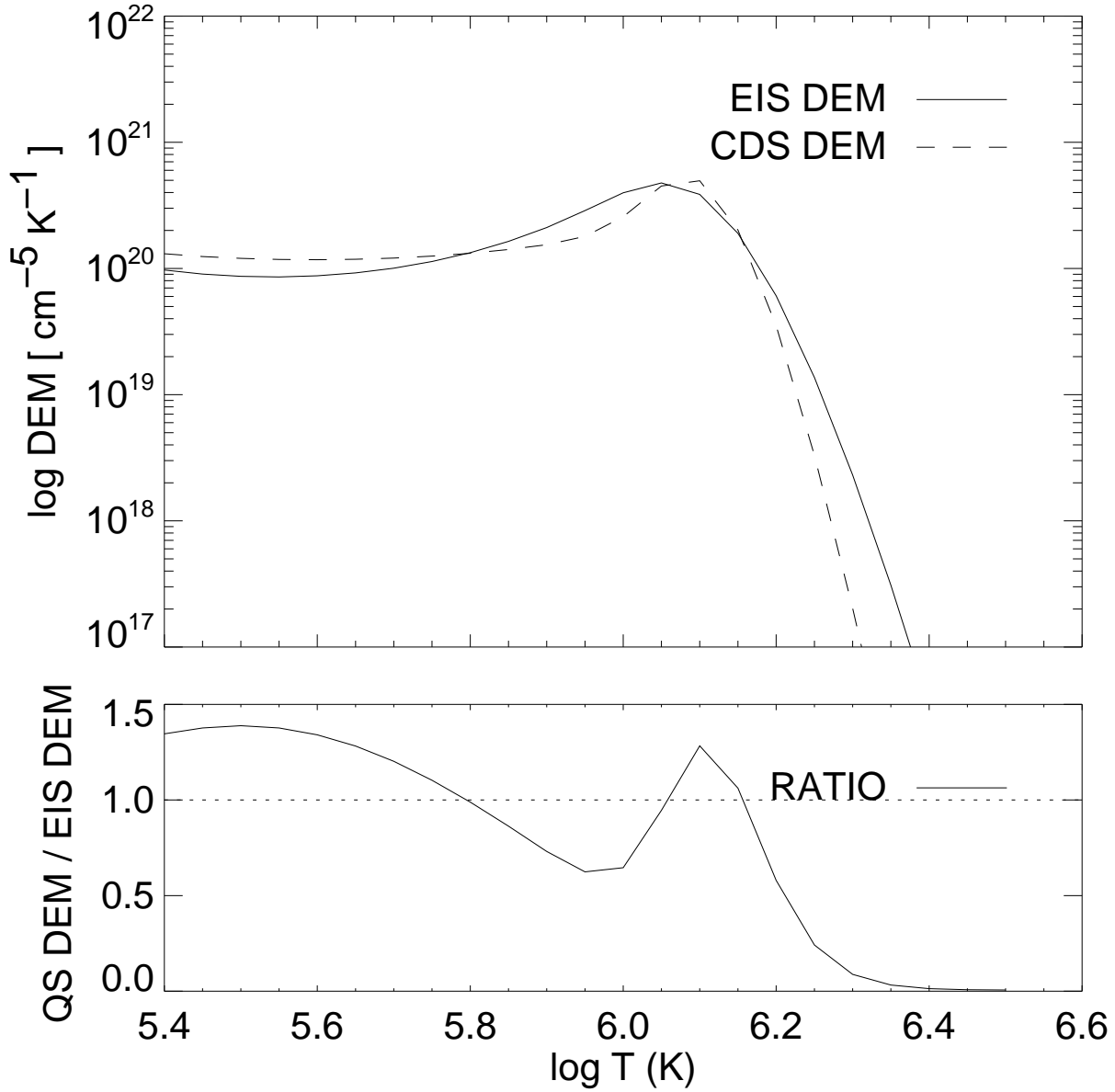


Fig. 4.— Comparison between the EIS best case DEM and the DEM for the quiet corona derived by Brooks & Warren (2006). The Ratio of the previous DEM to the EIS DEM is shown in the lower panel.

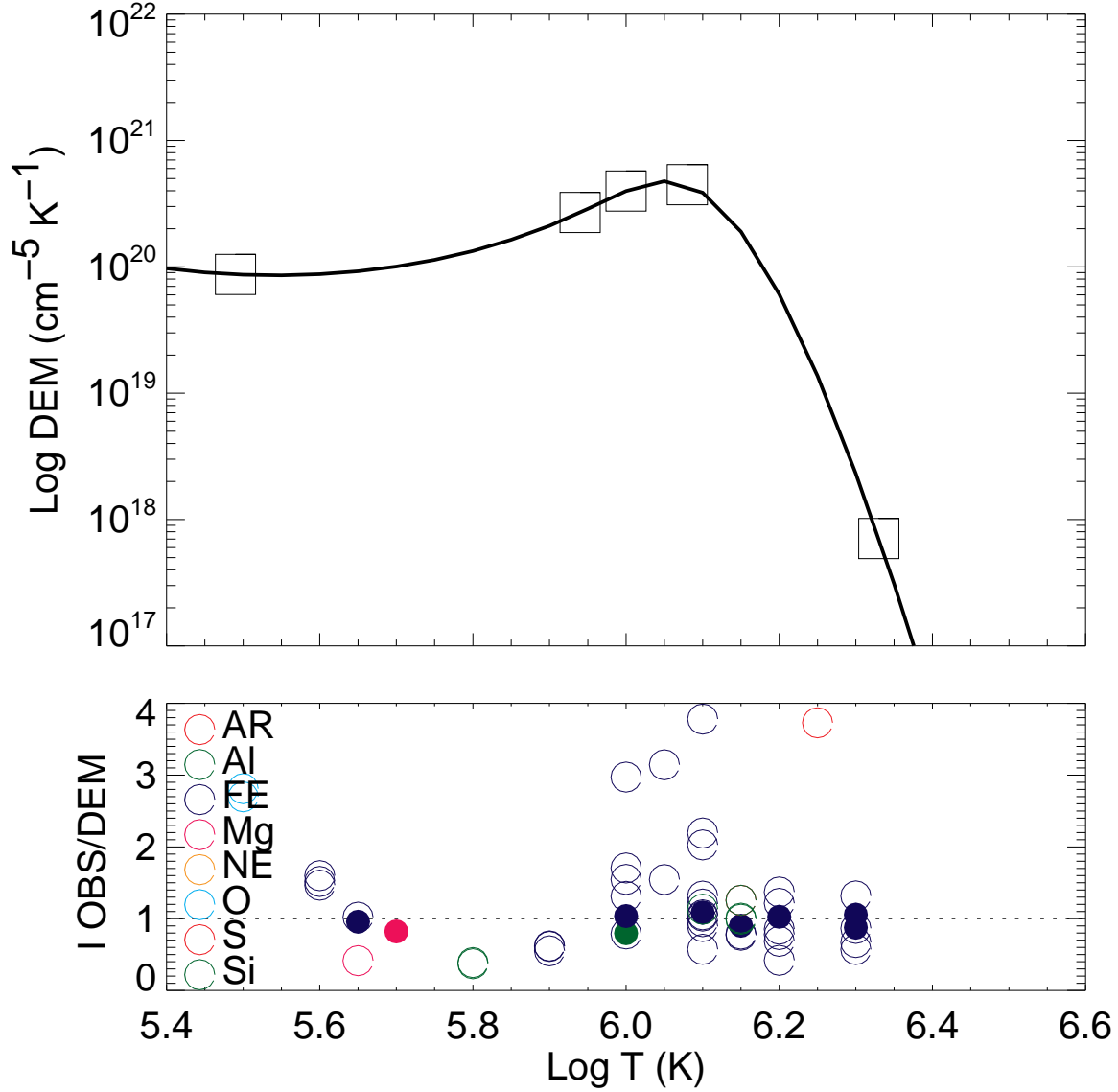


Fig. 5.— The DEM solution for all the spectral lines studied in this paper plotted as a function of temperature (upper panel). The squares show the positions of the spline knots. The lower panel shows ratios of the observed to DEM predicted intensities. Filled circles represent the lines retained to produce the subset and empty circles represent the lines that were deselected because there was a better candidate line available at the same temperature.

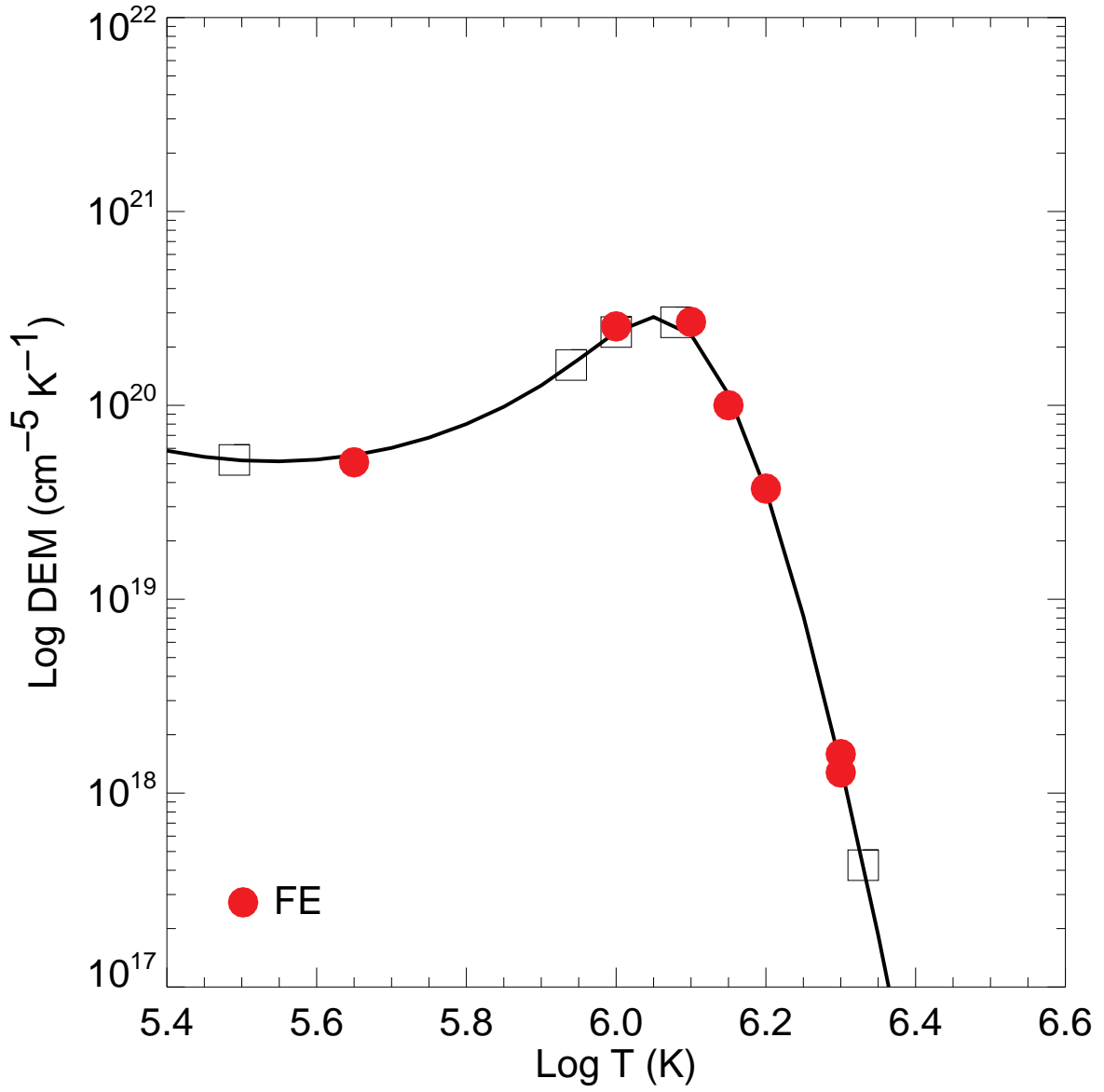


Fig. 6.— DEM distribution derived from a single EIS pixel.

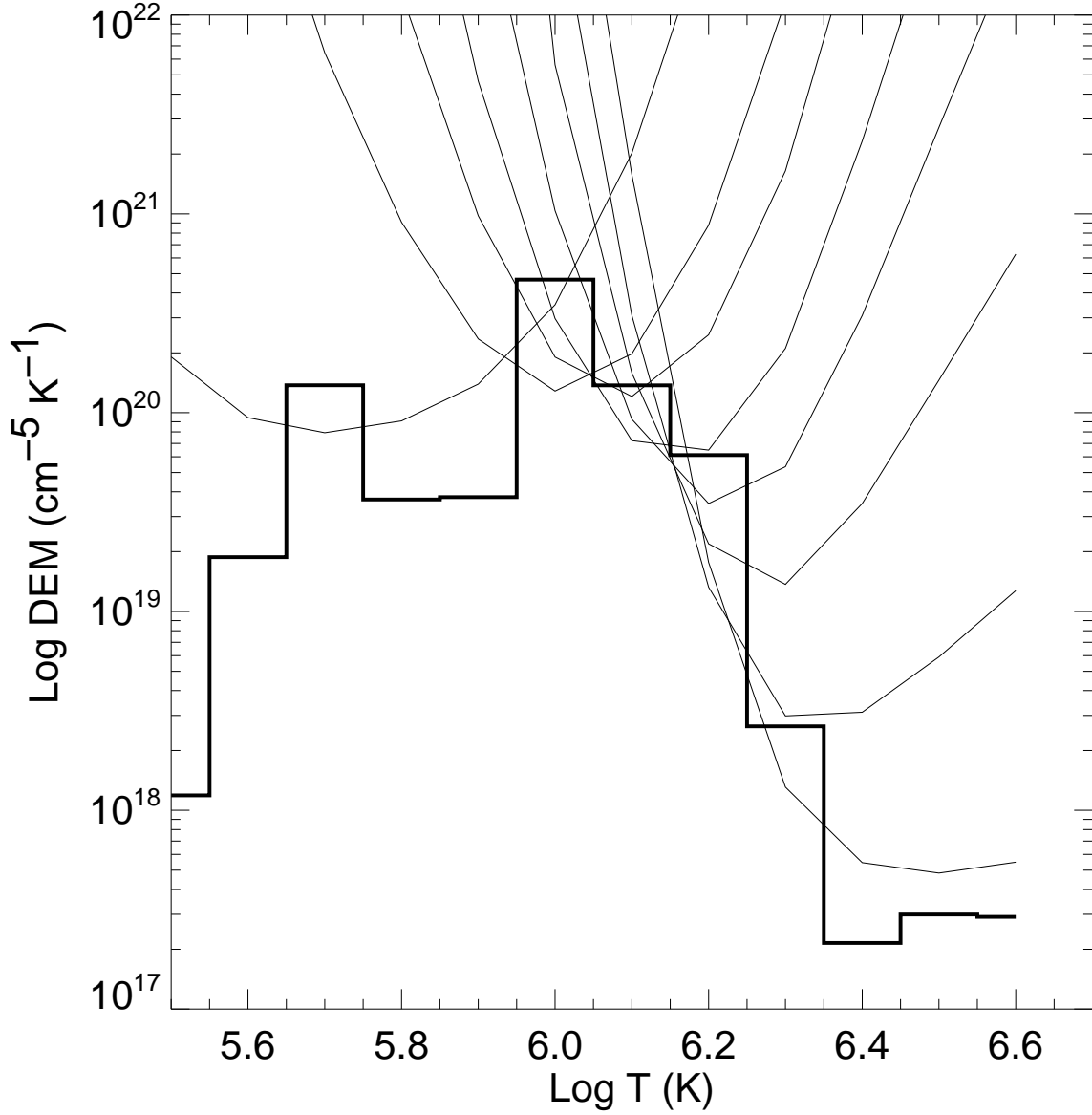


Fig. 7.— DEM distribution (histogram) derived from a single EIS pixel using the MCMC algorithm. DEM loci curves calculated for each line are also plotted.

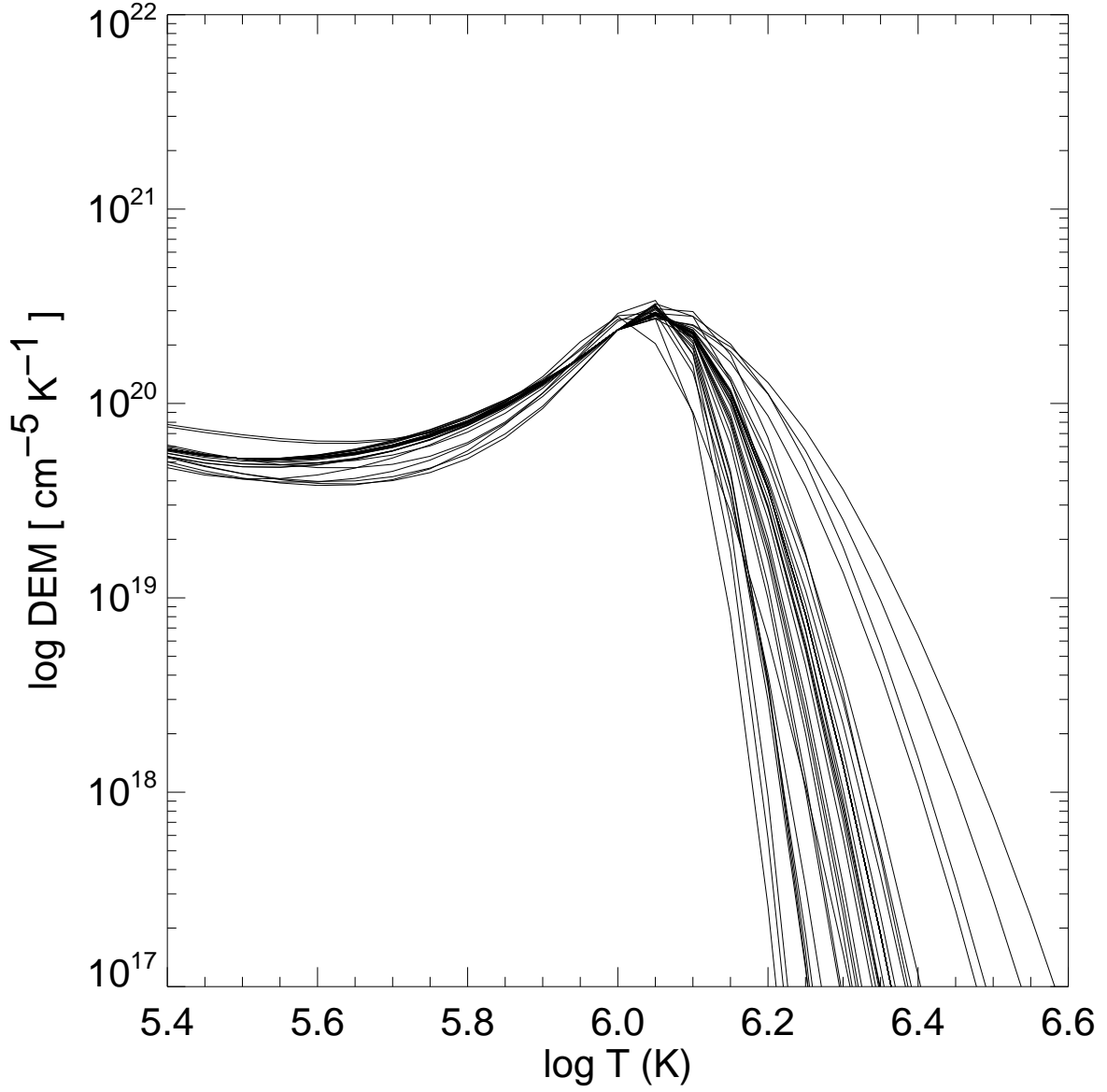


Fig. 8.— DEM solutions for all the datasets as a function of temperature. Note the similarity in shape.